

Design and Testing of a New Cell Microinjector Based on Small-Stiffness Mechanism*

Yuzhang Wei and Qingsong Xu
Department of Electromechanical Engineering
University of Macau, Macau, China
qsxu@um.edu.mo

Abstract—Cell microinjection is extremely crucial in biomedical domain. Currently, cell microinjection is mostly operated by manual method and position-based robotic method. However, the success rate and survival rate of the injected cells are relatively low. Force-assisted robotic cell microinjection can provide force feedback and protect the cells from excessive force. In this paper, a new cell microinjector with novel small-stiffness mechanism is proposed. The small-stiffness property is achieved by combining together a constant-force mechanism and small-stiffness mechanism with force intercept. The constant-force mechanism is used to offset the force intercept of the small-stiffness mechanism when the constant-force mechanism works at constant-force range. The constant-force mechanism is modeled, simulated, optimized, fabricated and calibrated. Results show that the designed constant-force mechanism can offset the intercept force well, because the variation of constant-force value is under 0.1 N during more than 1 mm constant-force motion range. The combined low-stiffness mechanism (without force intercept) can serve as an extremely sensitive force sensor for cell microinjection application.

I. INTRODUCTION

Cell microinjection usually adopts a fine needle to introduce small volume of extraneous materials into living cells [1]. Since the first-half of the last century, cell microinjection has found various applications in genetics, molecular biology, and other biomedical areas [2], [3]. The microinjection task has been implemented by many approaches [4]. Manual microinjection is a conventional method in biological research [5]. Nevertheless, it usually takes a long time (up to one year) to train an operator to become skilled in accomplishing such task [6]. Moreover, the success rate of injection for an experienced operator can only achieve about 15% because of the tough conditions to obtain a successful injection [7]. In order to overcome the shortcomings of manual injection, robotic cell injection has been introduced to achieve a higher success rate. Robotic microinjection utilizes automation technology to introduce materials into living cells with a fine needle.

Currently, contact-type microinjectors mainly contains optical microinjector [8], piezoresistive microinjector [9], piezoelectric microinjector [10], and capacitive microinjector [11]. These contact-type microinjectors with force sensing ability perceive microforce with extremely low stiffness but fragile

structures [12]. However, these structures have five common limitations. Firstly, the micropipette is directly bonded or fixed on microinjectors, making the replacement of broken micropipette being difficult or impossible. Secondly, they are so brittle that their stability and repeatability are greatly low. Thirdly, the travel range of microinjectors is relatively low, about dozens of micrometers, limited by their low stiffness structures. Fourthly, their fabrication process are very complicated and the cost is relatively high. The last but not least, the compressed air tube, for injecting quantitative volume materials, can't be connected with these microinjectors directly without affecting their performance.

To overcome the shortcoming of the current force-sensing microinjectors, the desired microinjector should satisfy several conditions. Firstly, the broken pipette should be able to be changed quickly. Secondly, the microinjector should have the ability to bear relatively large force to improve the stability. Thirdly, the travel range should be larger than 500 μm for injecting zebrafish embryo, which is a popular biological model with a diameter around 1 mm. Fourthly, the manufacturing process should better not be complicated and the cost should be low relatively. Fifthly, the compressed air tube should be easily connected with the microinjector.

The main contribution of the paper lies in the design and development of a new cell microinjector with novel small-stiffness mechanism. In the following sections of the paper, the design and analysis of the small-stiffness microinjector is introduced in Section II. The calibration of the new microinjector is reported in Section III. Section IV concludes the paper.

II. DESIGN AND ANALYSIS OF A NEW SMALL-STIFFNESS CELL MICROINJECTOR

Inspired by constant-force mechanism [13], [14], connecting positive-stiffness structure with negative-stiffness structure to obtain a zero-stiffness structure, a small-stiffness structure can be acquired with similar approach. However, the small-stiffness line has an intercept (denoted as F_b in Fig. 1(a) and (b)), that is, the force of small-stiffness structure is not begin with zero, preventing it from force sensor application. Thus, the intercept needs to be eliminated to obtain a small-stiffness force sensor. In order to offset the intercept, a zero-stiffness structure with the same value as the intercept of small-stiffness structure is adopted. These two structures are then combined together to produce a new small-stiffness

*This work was supported in part by the National Natural Science Foundation of China under Grant 51575545, the Macao Science and Technology Development Fund under Grant 179/2017/A3, and the Research Committee of the University of Macau under Grant MYRG2018-00034-FST to Q. Xu.

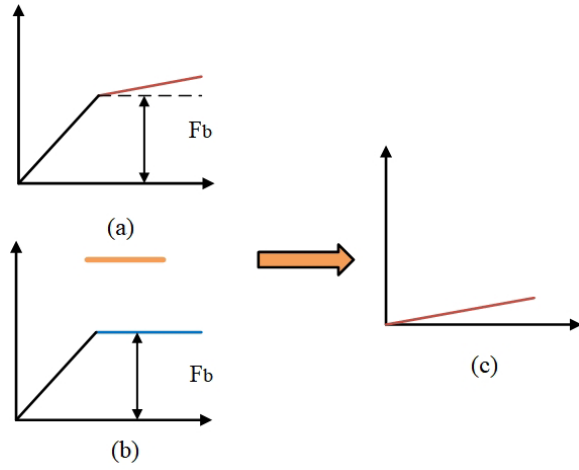


Fig. 1. Working principle of small-stiffness structure. (a) Small-stiffness mechanism with force intercept as F_b ; (b) Zero-stiffness mechanism with constant-force value as F_b ; (c) combining these two structures (a)-(b), and then zero-stiffness mechanism offsets the intercept F_b , generating a new small-stiffness mechanism.

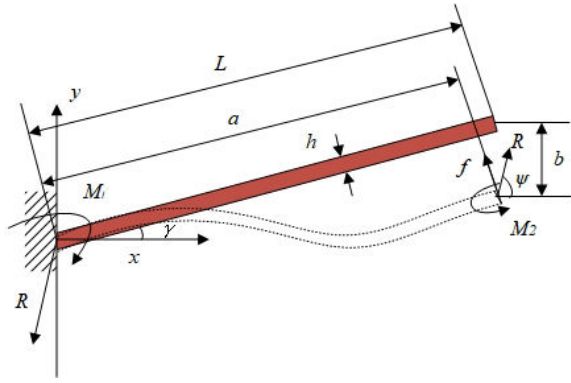


Fig. 2. The negative-stiffness structure, that is, fix-guided bistable beam, and related parameters of undeformed and deformed beam.

mechanism without intercept. In this way, the intercept can be simply and accurately offset during the half of constant-force range. In practice, a zero-stiffness structure should be designed firstly and then the small-stiffness structure with intercept can be adapted from the zero-stiffness structure.

A. Design of Zero-Stiffness Structure

The zero-stiffness structure is composed of negative-stiffness structure and positive-stiffness structure. Due to the fact that the property of negative-stiffness structure is easily affected by the parameter variation and meanwhile the variation is also limited, the negative-stiffness structure is designed first.

1) *Design of Negative-Stiffness Structure:* Currently, one popular negative-stiffness structure is the bistable beam [15]. A bistable beam is usually arranged at a tilted angle as fixed-guided beam, as shown in Fig. 2. When the bistable beam is deformed to some extent, buckling phenomenon and negative stiffness will occur. For convenience, the bistable beam will be adopted as the negative-stiffness structure.

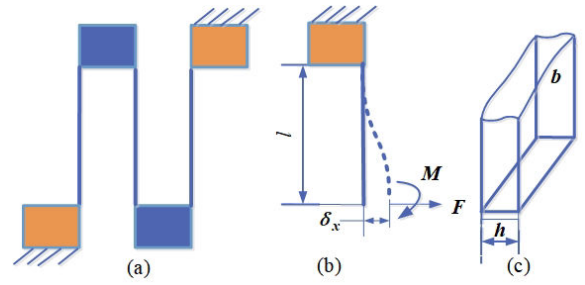


Fig. 3. The positive structure, that is, multi layer flexure. (a) 3 layers of MLF; (b) Single layer deformation under combined force and moment; (c) Related parameters.

In order to determine the parameters of the bistable beam, the analytical model is derived [13]. As the deflection of the bistable beam will generally deflect over 10%, large-deflection analytical method should be used, such as pseudo-rigid-body model (PRBM), elliptic integral method, and nonlinear finite element analysis. For convenience, the elliptic integral method is adopted in this work and related parameters are shown in Fig. 2. If the input deflection is given by (a, b) , the related governing equations for the large-deflection flexure can be deduced:

$$\sqrt{\alpha} = F(\kappa, \theta_1) - F(\kappa, \theta_2) \quad (1)$$

$$\frac{b}{L} = -\frac{1}{\sqrt{\alpha}} \{ 2\kappa \cos \psi (\cos \theta_1 - \cos \theta_2) + \sin \psi [2E(\kappa, \theta_2) - 2E(\kappa, \theta_1) - F(\kappa, \theta_2) + F(\kappa, \theta_1)] \} \quad (2)$$

$$\frac{a}{L} = -\frac{1}{\sqrt{\alpha}} \{ 2\kappa \sin \psi (\cos \theta_2 - \cos \theta_1) + \cos \psi [2E(\kappa, \theta_2) - 2E(\kappa, \theta_1) - F(\kappa, \theta_2) + F(\kappa, \theta_1)] \} \quad (3)$$

where $\alpha = (RL^2/EI)$, E represents the Young's modulus, and I denotes the second moment of area. Additionally, $F(\kappa, \theta)$ is the first-order incomplete elliptic integrals and $E(\kappa, \theta)$ is the second-order one, as shown below:

$$F(\kappa, \theta) = \int_0^\theta \frac{d\delta}{\sqrt{1 - \kappa^2 \sin^2 \delta}} \quad (4)$$

$$E(\kappa, \theta) = \int_0^\theta (\sqrt{1 - \kappa^2 \sin^2 \delta}) d\delta \quad (5)$$

where κ is the modulus of the above mentioned functions, which is a nondimensional parameter between 0 and 1. θ is the amplitude of the elliptic integral, affected by angle variable ϕ , the relationship between θ and ϕ is given as follows:

$$\kappa \sin \theta_1 = \cos \left(\frac{\psi - \phi_1}{2} \right) \quad (6)$$

$$\kappa \sin \theta_2 = \cos \left(\frac{\psi - \phi_2}{2} \right) \quad (7)$$

Considering the boundary conditions, that is, $\phi_1 = \phi_2 = 0$, the equations of the first and second buckling modes of the negative-stiffness beam can be deduced as follows.

$$\theta_2 = \pi - \theta_1 \quad (8)$$

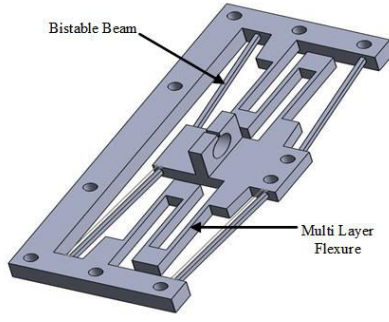


Fig. 4. 3D model of designed constant-force mechanism, composed of positive-stiffness structure, e.g., multi layer flexure, and negative-stiffness structure, e.g., bistable beam.

$$\theta_2 = 2\pi + \theta_1 \quad (9)$$

The first mode solution and second mode solution represent one inflection point and two injection points of the flexure deflection, respectively. By solving these equations, the solution of κ , R , and ψ can be deduced within one solution mode. Eventually, the negative driving force can be obtained:

$$f = R(\cos \psi \sin \gamma + \sin \psi \cos \gamma) \quad (10)$$

2) *Design of Positive-Stiffness Structure:* Currently, there are many positive-stiffness structures, such as slender leaf flexure, folded leaf flexure [14], and multi-layer flexure (MLF) [13]. Slender leaf flexure has the shortcoming of large size and stress stiffening phenomenon. Folded leaf flexure is weak in modularization, because it has three layers in a single modulus, deteriorating the flexibility in design. In this work, the multi layer flexure has been chosen owing to its modularity and flexibility, as shown in Fig. 3(a). The number of layers of MLF can be set as any positive integer and one layer acts as an independent module. These features make MLF be suitable for positive-stiffness structure.

The MLF has N same layers and each layer serves as a fixed-guided beam. Every beam is under the influence of combined force F and moment M , as shown in Fig. 3(b). As the beam is guided into one direction, the rotational angle of the end of the flexure should be zero.

According to the boundary conditions, the following equations are obtained based on mechanics of materials.

$$\frac{Fl^2}{2EI} - \frac{Ml}{EI} = 0 \quad (11)$$

$$\frac{Fl^3}{3EI} - \frac{Ml^2}{2EI} = \delta_x \quad (12)$$

where l denotes the length of flexure, δ_x is the displacement of fixed-guided beam, E represent Young's modulus, b and h denote the width and height of the flexure, respectively. Additionally, $F = F_x/2$ denotes the force relationship and $I = bh^3/12$ represent the inertial moment of cross-sectional area, as Figure 3(c) shows.

Solving (11) and (12), obtains

$$\delta_x = \frac{Fl^3}{12EI} \quad (13)$$

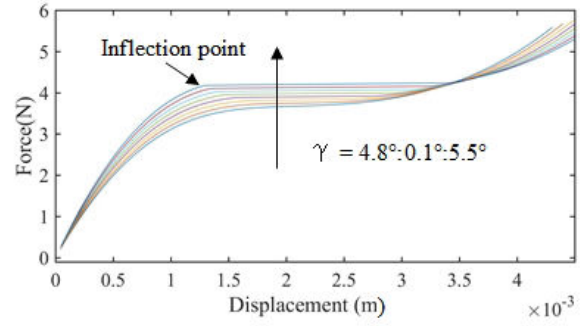


Fig. 5. Force-displacement relationship of constant-force mechanism with analytical model with angle variation.

The positive-stiffness of MLF can be deduced:

$$K = \frac{F}{N\delta_x} = \frac{Ebh^3}{Nl^3} \quad (14)$$

3) *Parameter Design of Zero-stiffness Mechanism:* The negative-stiffness structure and positive-stiffness structure have been selected and modeled as above. In the final step of design, the zygomorphous structure is chosen in view of stability and load bearing. Moreover, two negative-stiffness beams are selected for improving the guiding stability, because the transverse displacement will easily occur with only one negative-stiffness beam. The final structure of the constant-force mechanism is shown in Fig. 4.

As mentioned earlier, due to the fact that the parameters of the negative-stiffness structure are more influential and have relatively limited ranges, the parameters of the negative-stiffness structure should be designed first. Owing to the microinjection application and the design of intercept offsetting, the travel range of constant-force range should be as large as possible. According to the previous work [13], [16], the length of the bistable beam (denoted as L in Fig. 2), and the inclined angle (denoted as γ in Fig.2) have positive correlation with the travel range of constant force. The in-plane width of the bistable beam (denoted as h in Fig.2) has negative correlation with the travel range of constant-force mechanism. However, these parameters are limited by the manufacturing conditions, compactness, and feasibility of physics.

Although the in-plane width (h) has negative correlation with the travel range of constant-force mechanism, the minimum value of the width is limited by the manufacturing process. Meanwhile, the load bearing ability should also be considered for the concerned application. In order to achieve rapid prototyping, 3D printer (model: uPrint SE Plus, from Stratasys Ltd, Eden Prairie, MN, USA) is used in this work. Taking the load bearing ability and minimum width that can be afforded by the 3D printer, 1 mm is selected as the in-plane width of the negative-stiffness beam.

Although the angle of inclined negative-stiffness beam (γ) has positive correlation with the travel range of constant-force mechanism, the maximum value of the angle is limited by the axial compression. As shown in Fig. 5, when the inclined angle varies from 4.8° to 5.5° with other parameters as final

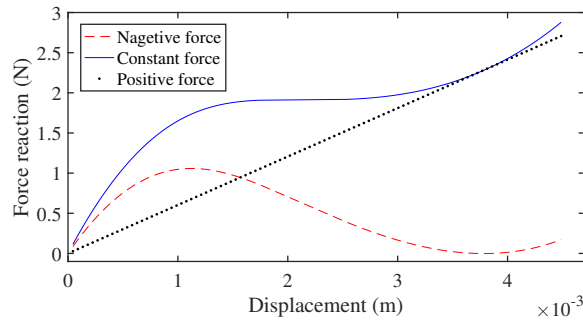


Fig. 6. Force-displacement relationship of constant-force mechanism and the two-component mechanism obtained by analytical model with optimized parameters. The constant-force value is about 1.91 N with constant-force range of 1 mm (5% interval of force variation).

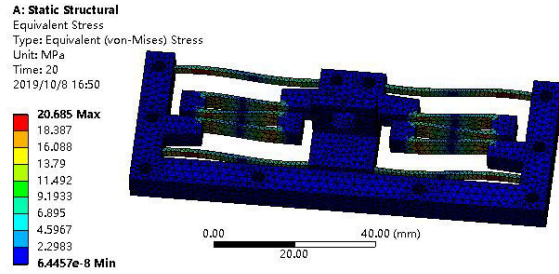


Fig. 7. FEA simulation result of stress distribution.

designed parameters, an inflection point occurs at the force-displacement curve which is obtained by the analytical model with the angle varies from 5.1° to 5.5° . Meanwhile, the value of constant force remains the same value, which is unrealistic. However, the value of constant force from analytical model is greatly different from that of FEA simulation. Generally, the value of the FEA simulation is taken as “real” value, and then these curves with inflection points will not be considered. The inflection point may be caused by large axial compression (more than 10%). Consequently, the value of angle for the negative-stiffness beam is selected as 5° .

Since the in-plane width and inclined angle have been determined, the length and out-plane thickness of the negative-stiffness beam and those of positive-stiffness beam should also be confirmed. As the material to be used in 3D printer has low yield strength (ABS Plus, Young’s modulus: 2.2 Gpa, yield strength: 31 Mpa), the safety factor should be guaranteed above 1. At the same time, the feature of constant force should also be ensured. Consequently, four parameters need to be coordinated to satisfy two objectives, which is a typical problem of multi objective optimal. For this case, the primary 3D model in Fig. 4 is firstly parameterized and exported to ANSYS workbench with Multi Objective Genetic Algorithm (MOGA). The MOGA method is a variant of the popular NSGA-II (Non-dominated Sorted Genetic Algorithm-II) based on controlled elitism concepts. It supports multiple objectives and constraints, and aims at finding the global optimum.

Before the optimization in MOGA, parameter searching has been conducted in MATLAB through analytical model for

TABLE I
MAIN PARAMETERS OF CONSTANT-FORCE MECHANISM.

Componet	Parameter	Value
Positive-stiffness beam	l	18.25mm
	h	1mm
	b	5mm
Negative-stiffness beam	L	36.5mm
	γ	5°
	h	1mm
	w	2mm

narrowing the ranges of parameters that need to be screened. Thus, the analytical model not only can be verified for FEA simulation, but also can help accelerating the optimization. It also should be noted that the manufacturing accuracy of the adopted 3D printer is 0.25 mm. Therefore, the parameters for optimization is discrete. In order to improve the efficiency, the optimization objective of constant force feature is solved by minimizing the difference between the force value of a point (F_1) of head end and force value of another point (F_2) of tail end. These two end points are selected by experience.

As mentioned above, two objectives need to be optimized: $F_1 - F_2 = 0$ and *Safety factor* > 1 . The length variation range of the positive-stiffness beam is 14 : 0.25 : 19 mm, the variation range for the length of negative-stiffness beam is 31 : 0.25 : 39 mm, the variation range of out-plane thickness of the positive-stiffness beam is 2 : 0.25 : 6 mm, and the variation range of out-of-plane thickness of the negative-stiffness beam is 0.5 : 0.5 : 5.5 mm. After optimization through MOGA, parameters of the difference value below 0.1 mm are selected manually by conducting FEA simulation through ANSYS Workbench. The optimized parameters are given in Table I. The force-displacement relationship of constant-force mechanism and the two-component mechanism with these optimized parameters (positive- and negative-stiffness) are shown in Fig.6. The constant-force value is about 1.91 N with constant-force range of 1.21 mm (force variation below 0.1 N). It also should be noted that the force value only represents half of total structure in Fig. 4.

In order to verify the optimized results, FEA simulation through ANSYS workbench is conducted, as shown in Fig. 7. The maximum stress, reached at maximum displacement of 4 mm, is 20.685 MPa, and the yield strength of ABS Plus for 3D printing is 31 MPa. Thus, the safety factor is 1.50, which is a satisfying result. The force values from mathematical model and FEA simulation are also shown in Fig. 8. The analytical model result of constant-force value is 3.82 N with 1.21 mm constant-force range. The FEA simulation result of constant-force value is 3.55 N with 1.30 mm constant-force range, producing a 7% deviation. The deviation may be caused by the simplification in analytical modeling. In general, the deviation is acceptable and these results are in good agreement.

B. Design of Small-Stiffness Structure

The zero-stiffness structure, e.g., constant-force mechanism, is used to offset the intercept force of the small-stiffness structure. In other word, the small-stiffness structure can be

TABLE II
MAIN PARAMETERS OF SMALL-STIFFNESS MECHANISM.

Component	Parameter	Value
Positive-stiffness beam	l	18.5mm
	h	1mm
	b	5.25mm
Negative-stiffness beam	L	36.5mm
	γ	5°
	h	1mm
	w	2mm

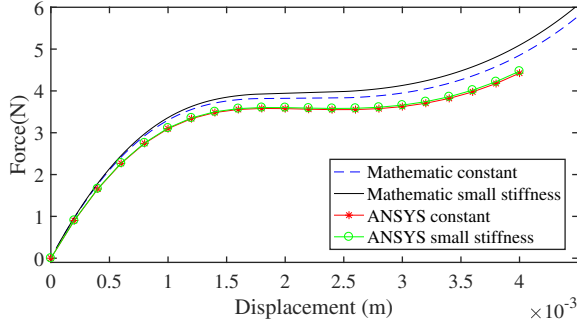


Fig. 8. Force-displacement relationships of constant-force mechanism and small-stiffness mechanism obtained by mathematical model and ANSYS simulation.

adapted from zero-stiffness by increasing the positive stiffness suitably. According to (14), a small stiffness can be obtained by increasing the width b and meanwhile increasing the length l with minimum manufacturing accuracy of 3D printer, i.e., 0.25mm. The final parameters can be seen in Table II. The mathematical model and FEA simulation results (ANSYS) are presented in Fig. 8. It is found that the force values of small-stiffness mechanism are slightly larger than that of constant-force mechanism in both results.

Eventually, the constant-force mechanism and small-stiffness mechanism with force intercept are moved relatively to each other with the same designed distance, making the zero-stiffness structure arriving at near the middle point of constant-force range. In this way, the intercept can be offsetted simply and accurately during the half of constant force range. Consequently, a small-stiffness cell microinjector can be made.

III. EXPERIMENTAL RESULTS

A. Calibration Experimental Setup

In order to test the performance of the constant-force mechanism and small-stiffness mechanism, calibration experiments are conducted. The prototype is manufactured by a 3D printer (model: uPrint SE Plus, from Stratasys Ltd.) with the material of ABS Plus. The experimental setup can be seen in Fig. 9. The constant-force mechanism is fixed on a vibration isolation platform and driven by an XYZ stage manually. The driving force signal is measured by a force sensor (model: LSB200, from FUTEK Advanced Sensor Technology, Inc.). The output displacement is measured with a laser displacement sensor (model: LK-H055, from Keyence Corp.). Besides, a real-time controller (model: PXIe-1082, from National Instruments

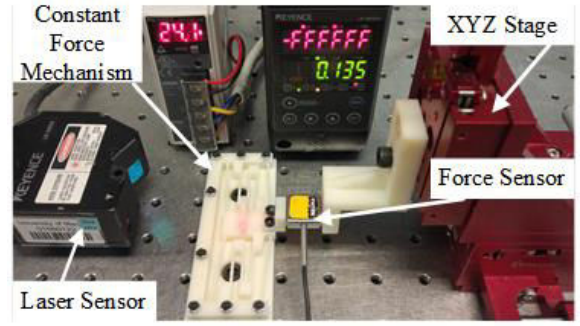


Fig. 9. The calibration setup for constant-force mechanism and small-stiffness mechanism.

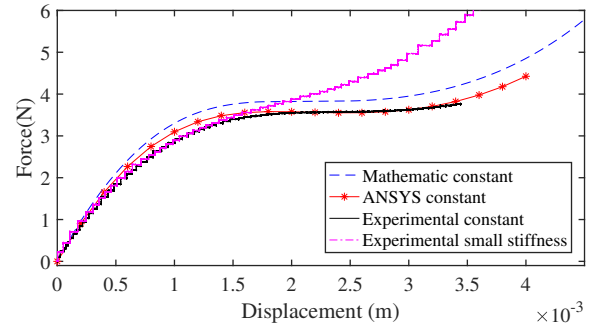


Fig. 10. Experimental calibration results of constant-force mechanism.

Corp.) is used to collect signals.

B. Calibration Experimental Results of Constant-Force Mechanism

As shown in Fig. 10, the experimental result of constant-force value is 3.56 N and the constant-force range is 1.13 mm. The deviation between the mathematical model and experimental results is about 7% for the constant-force value and constant-force range. The deviation between the FEA simulation and experimental results is very small, as shown in Table III. To conclude, the deviation is acceptable, because the constant-force mechanism is used to offset the intercept force for the small-stiffness mechanism. The only thing needs to be considered is that the range of constant force is large enough. The half of constant-force range for experiment is 0.565 mm, which is larger than the radius of normal zebrafish embryo, that is, 0.5 mm. Consequently, the constant-force mechanism is satisfying for building a microinjector.

C. Calibration Experimental Results of Small-Stiffness Mechanism

The small-stiffness mechanism is modified from zero-stiffness mechanism (constant-force mechanism) by increasing positive stiffness. The calibration setup is similar to that of the zero-stiffness mechanism. The calibration result is given in Fig. 10. The small stiffness has the force intercept value that is the same as the constant-force mechanism and a small slope. According to Fig. 10, $\Delta x = 1.13$ mm and $\Delta y = 4.715 - 3.505 = 1.21$ N. Thus, the slope is 1.07 N/mm. In this way, the

TABLE III
ANALYTICAL MODEL, FEA SIMULATION AND EXPERIMENTAL RESULTS
OF THE CONSTANT-FORCE PERFORMANCE

Methods	Constant-force value	Constant-force range
Mathematical model	3.82 N	1.21 mm
FEA simulation	3.55 N	1.30 mm
Experimental result	3.56 N	1.13 mm

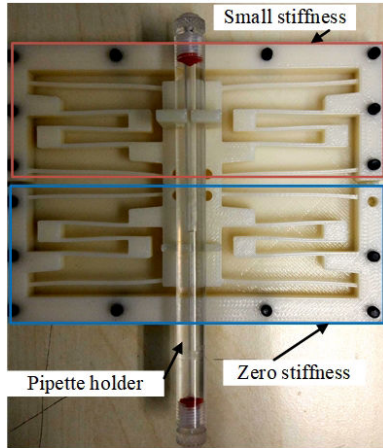


Fig. 11. Prototype microinjector based on small-stiffness mechanism.

zero-stiffness mechanism can offset the force intercept of the small-stiffness mechanism, generating a new small-stiffness mechanism, as illustrated in Fig. 1(c).

D. Assembled Microinjector

The new microinjector is composed of the zero-stiffness mechanism and small-stiffness mechanism. Equal pre-deformation is exerted by fixing them on the designed location, where zero-stiffness and small-stiffness mechanisms are at middle point of the constant-force range as shown in Fig. 11. In this way, the constant force of zero-stiffness can offset the intercept force of the small-stiffness mechanism. This microinjector can be used to change the broken pipette easily by using the commercial pipette holder. Moreover, the stability of the microinjector is very well, because it can bear a force of several Newton. Furthermore, the travel range is about 556 μm , which is enough for injecting zebrafish embryo. Additionally, the fast prototype by 3D printer is very economical and simple. Besides, the compressive air tube can be easily attached to the microinjector. The test of microinjector will be conducted in the future work.

IV. CONCLUSION

In this paper, a new cell microinjector with novel small-stiffness mechanism is presented. The small-stiffness mechanism is realized by combining a zero-stiffness mechanism (constant-force mechanism) with a small-stiffness mechanism with force intercept. The zero-stiffness mechanism is used to offset the force intercept, making the whole mechanism a small-stiffness mechanism without force intercept. This kind

of mechanism could be used to perceive micro-force during microinjection. The constant-force mechanism is modeled, simulated, optimized, fabricated and calibrated in this paper. The results show that the mathematical model, ANSYS simulation and experimental results are in good agreement. Moreover, the variation of the constant-force value during more than 1 mm constant-force range is under 0.1 N. The flatness feature will benefit in offset the force intercept. In the future work, piezoresistive strain gauge and other high precision force sensing elements would be attached to the small-stiffness microinjector to perceive the microinjection force during cell microinjection.

REFERENCES

- [1] Y. Zhang, K. K. Tan, and S. Huang, "Vision-servo system for automated cell injection," *IEEE Transactions on Industrial Electronics*, vol. 56, no. 1, p. 231, 2009.
- [2] D. Desmaële, M. Boukallel, and S. Régner, "A planar structure sensitive to out-of-plane forces for the force-controlled injection of suspended and adherent cells," in *Engineering in Medicine and Biology Society, EMBC, 2011 Annual International Conference of the IEEE*, 2011, pp. 8420–8423.
- [3] T. Beutel, N. Ferreira, A. Balck, M. Leester-Schadel, and S. Buttgenbach, "Cell manipulation system based on a self-calibrating silicon micro force sensor providing capillary status monitoring," *IEEE Sensors Journal*, vol. 12, no. 10, pp. 3075–3081, 2012.
- [4] Q. Xu, *Micromachines for Biological Micromanipulation*. Springer, 2018.
- [5] W. Wang, X. Liu, D. Gelinas, B. Ciruna, and Y. Sun, "A fully automated robotic system for microinjection of zebrafish embryos," *PLoS one*, vol. 2, no. 9, p. e862, 2007.
- [6] A. Ghanbari, B. Horan, S. Nahavandi, X. Chen, and W. Wang, "Haptic microrobotic cell injection system," *IEEE Systems Journal*, vol. 8, no. 2, pp. 371–383, 2014.
- [7] H. Ladjal, J.-L. Hanus, and A. Ferreira, "Micro-to-nano biomechanical modeling for assisted biological cell injection," *IEEE Transactions on Biomedical Engineering*, vol. 60, no. 9, pp. 2461–2471, 2013.
- [8] O. Loh, R. Lam, M. Chen, N. Moldovan, H. Huang, D. Ho, and H. D. Espinosa, "Nanofountain-probe-based high-resolution patterning and single-cell injection of functionalized nanodiamonds," *Small*, vol. 5, no. 14, pp. 1667–1674, 2009.
- [9] V. T. Stavrov, A. A. Shulev, C. M. Hardalov, V. M. Todorov, and I. R. Roussev, "All-silicon microforce sensor for bio applications," in *Smart Sensors, Actuators, and MEMS VI*, vol. 8763, 2013, p. 87630Y.
- [10] A. Pillarisetti, M. Pekarev, A. D. Brooks, and J. P. Desai, "Evaluating the effect of force feedback in cell injection," *IEEE Transactions on Automation Science and Engineering*, vol. 4, no. 3, pp. 322–331, 2007.
- [11] Y. Sun, B. J. Nelson, D. P. Potasek, and E. Enikov, "A bulk microfabricated multi-axis capacitive cellular force sensor using transverse comb drives," *Journal of Micromechanics and Microengineering*, vol. 12, no. 6, p. 832, 2002.
- [12] Y. Wei and Q. Xu, "A survey of force-assisted robotic cell microinjection technologies," *IEEE Transactions on Automation Science and Engineering*, 2018.
- [13] Q. Xu, "Design of a large-stroke bistable mechanism for the application in constant-force micropositioning stage," *Journal of Mechanisms and Robotics*, vol. 9, no. 1, p. 011006, 2017.
- [14] X. Zhang, G. Wang, and Q. Xu, "Design, analysis and testing of a new compliant compound constant-force mechanism," in *Actuators*, vol. 7, no. 4. Multidisciplinary Digital Publishing Institute, 2018, p. 65.
- [15] Y. Liu, Y. Zhang, and Q. Xu, "Design and control of a novel compliant constant-force gripper based on buckled fixed-guided beams," *IEEE/ASME Transactions on Mechatronics*, vol. 22, no. 1, pp. 476–486, 2016.
- [16] P. Wang and Q. Xu, "Design and modeling of constant-force mechanisms: A survey," *Mechanism and Machine Theory*, vol. 119, pp. 1–21, 2018.